Numerical model of harmonic Hall voltage detection for spintronic devices

Sławomir Ziętek [1,*] Jakub Mojsiejuk [1,†] Krzysztof Grochot [1,2] Stanisław Łazarski [1]
Witold Skowroński [1] and Tomasz Stobiecki [1,2]

[1]*Institute of Electronics, AGH University of Science and Technology, Aleja Adama Mickiewicza 30, 30-059 Kraków, Poland*
[2]*Faculty of Physics and Applied Computer Science, AGH University of Science and Technology, Aleja Adama Mickiewicza 30,
30-059 Kraków, Poland*

We present a numerical macrospin model for harmonic voltage detection in multilayer spintronic devices. The core of the computational backend is based on the Landau-Lifshitz-Gilbert-Slonczewski equation, which combines high performance and satisfactory agreement with the experimental results in large-scale applications. We compare the simulations with the experimental findings in a Ta/CoFeB bilayer system for angular- and magnetic-field-dependent resistance measurements, electrically detected magnetization dynamics, and harmonic Hall voltage detection. Using simulated scans of the selected system parameters such as the polar angle θ, magnetization saturation ($\mu_0 M_s$), or uniaxial magnetic anisotropy (K_u), we show the resultant changes in the harmonic Hall voltage, demonstrating the dominating influence of the $\mu_0 M_s$ on the first and second harmonics. In the spin-diode ferromagnetic resonance method, the ($\mu_0 M_s$, K_u) parameter space may be optimized numerically to obtain a set of viable curves that fit the experimental data.

I. INTRODUCTION

The development of novel electronic devices utilizing electron spin for their operation has become an increasingly important branch of science and engineering in the past decade [1–4]. Specifically, taking advantage of both the electron spin and charge creates an opportunity for further miniaturization and increase in the energy efficiency [5] of the electronic devices. However, experimental investigations typically require expensive and time-consuming fabrication processes as well as a unique measurement methodology. Computer-aided optimization of spintronics devices, coupled with the prediction of their electric and magnetic properties, vastly reduces the number of experimental iterations and allows a faster and more efficient prototype device development. In addition, modeling of multilayer devices enables the extraction of parameters that are typically hard to obtain from experiments.

After the experimental discovery of the so-called spin-orbit torque (SOT) [6–12], there have been numerous studies on spin current generation in nonmagnetic materials with high spin-orbit coupling additionally improved by interfacial effects [13,14]. Utilizing SOT may lead to fast magnetization switching [15] and more durable magnetic memory design [16]. To quantify the efficiency of the effect, typically called the spin-Hall angle, one computes the ratio of the spin current to the charge current. In recent years, there has been a sprout in the development of spin-Hall angle measurement techniques such as spin-torque ferromagnetic resonance (ST-FMR) [17], magnetization switching induced by current [18], and harmonic Hall voltage detection [19,20]. The latter method does not require a sophisticated fabrication protocol, nor the determination of additional thermal or high-frequency effects, and allows for the extraction of dampinglike and fieldlike effective fields, from which the spin-Hall efficiencies may be calculated.

In this work, we employ the SOT effect as a basis for the electrical model that simulates the harmonic Hall voltage technique using fieldlike (FL) and dampinglike (DL) SOT torques. Furthermore, we present highly efficient macrospin modeling software for the electrical detection of static and dynamic magnetic properties in multilayer spintronic devices. The software numerically solves the Landau-Lifshitz-Gilbert-Slonczewski (LLGS) equation using a dedicated c++ engine and enables simulations of the magnetization, magnetoresistance, ferromagnetic resonance, and harmonic Hall voltage measurements of the multilayer system simultaneously as a function of the magnetic field amplitude and angle with respect to the anisotropy axis direction. Our model demonstrates good agreement with the experimental data and provides additional insights into different aspects of magnetization dynamics and harmonic Hall measurement.

Moreover, we show the dependence of magnetization, saturation, and anisotropy on the harmonic Hall voltage detection, with the former having a much stronger impact on the final result. The model package, called CMTJ (C++ Magnetic Tunnel Junctions), is provided in both c++ and PYTHON interfaces, along with the hereby described postprocessing steps. As a demonstration of the ease of use and the speed of the model, all simulations conducted in this article may be reproduced within a half-hour on a modern laptop. The simulation scripts along with the simulation package itself are open source; see Ref. [21].

*zietek@agh.edu.pl
†mojsieju@agh.edu.pl

II. NUMERICAL MODEL OF ELECTRICAL DETECTION

A. Theoretical background

First, we present a theoretical model of the magnetization dynamics together with the electrical detection methodology. We adapt the standard Landau-Lifshitz-Gilbert-Slonczewski (LLGS) equation, like presented in, e.g., Nguyen *et al.* [22], into LL form [6], such that it may be implemented in the numerical engine. The LLGS equation itself is given in the form

$$\frac{d\mathbf{m}}{dt} = -\gamma_0 \mathbf{m} \times \mathbf{H}_{\mathrm{eff}} + \alpha_{\mathrm{G}} \mathbf{m} \times \frac{d\mathbf{m}}{dt} \\ - \gamma_0 |H_{\mathrm{FL}}|(\mathbf{m} \times \mathbf{p}) - \gamma_0 |H_{\mathrm{DL}}|(\mathbf{m} \times \mathbf{m} \times \mathbf{p}), \quad (1)$$

where $\mathbf{m} = \frac{\mathbf{M}}{\mu_0 M_s}$ is the normalized magnetization vector with $\mu_0 M_s$ as the magnetization saturation, α_{G} is the dimensionless Gilbert damping parameter, $\mathbf{H}_{\mathrm{eff}}$ is the effective field vector, $\mathbf{p}$ is the polarization vector, and γ_0 is the gyromagnetic factor. The terms representing the magnitude of the H_{FL} (fieldlike) and H_{DL} (dampinglike) torque fields have a concrete connection with the spin-Hall angle and correspond to the DL and FL SOT. See the Appendix for more details on the transition from the LLGS form to the numerically viable LL form. The effective field vector $\mathbf{H}_{\mathrm{eff}}$ is usually composed of various field contributions, which, depending on the context of the simulation, may be added or disabled. The simulation package in question already provides a range of such contributions, including the interlayer exchange coupling (IEC), dipole and demagnetization interactions, magnetic anisotropy, and external magnetic field contribution. In the experimental data, presented in the following sections, we investigate a bilayer (heavy metal/ferromagnet) structure, and thus we may omit IEC and dipole interactions in our simulations. For numeric integration, we employ the higher-order Runge-Kutta method. After each integration step, the $\mathbf{m}$ vectors are normalized to avoid cumulative numerical error. In deciding on the value of the integration step, we usually compromise the computation time and the stability of the numerical solution. For the majority of the simulations, this parameter is in the range of a femtosecond or lower. As a good rule of thumb, it is better to start at a lower value (around 10^{-13} s) and steadily increase it, verifying that the obtained results are still consistent.

B. Modeling of magnetoresistance effects

In our simulations, we can easily compute longitudinal (R_{xx}) and transverse (R_{xy}) magnetoresistance loops for current in-plane (CIP) and current perpendicular to the plane (CPP) configurations [see Figs. 1(d) and 1(e)], as a function of the magnetic field magnitude or angle. To obtain R_{xx} and R_{xy} loops, we adopt a model from [23], given by Eqs. (2) and (3),

$$R_{\mathrm{xx}} = R_{\mathrm{xx0}} + \left(\Delta R_{\mathrm{AMR}} m_x^2 + \Delta R_{\mathrm{SMR}} m_y^2 \right), \quad (2)$$

$$R_{\mathrm{xy}} = R_{\mathrm{xy0}} + \frac{1}{2} \Delta R_{\mathrm{AHE}} m_z + \frac{w}{l} (\Delta R_{\mathrm{SMR}} + \Delta R_{\mathrm{AMR}}) m_x m_y, \quad (3)$$

where ΔR_{AMR} and ΔR_{SMR} are the magnitudes of the anisotropic (AMR) and spin-Hall (SMR) magnetoresistances (both in Ω) in the R_{xx} configuration. ΔR_{AHE} is the magnitude
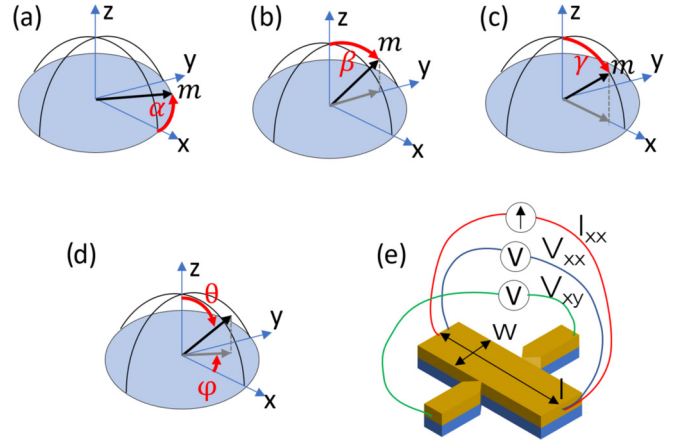

FIG. 1. The reference diagram for measurement arrangements used in this work. (a)–(c) The angles α, β, γ used in simulations and experiment in the saturating field. The angle θ is taken to be the polar angle and ϕ is the azimuthal angle (d). (e) The application of the voltmeter in the measurement.

of the anomalous Hall effect (AHE) (also in ohms), l is the length, and w is the width of the sample. In the dynamic state, the resistance is calculated as a function of time and then used for the calculation of ST-FMR and harmonic Hall voltages.

C. Spin-diode ferromagnetic resonance (SD-FMR)

In addition to the inductive and optical magnetometry methods, SD-FMR has proven to be a powerful experimental tool in the study of magnetization dynamics in microwave spintronic devices such as oscillators or detectors [24]. When the alternating current (AC) is passed through a magnetoresistive element, it generates small changes of magnetization driven by secondary effects of the Oersted field, spin transfer torque (STT), or SOT, which finally lead to the oscillations of resistance [25]. Mixing of the AC and oscillating resistance gives rise to the mixing voltage, which has both direct current (DC) and AC components at the first ($f' = f$) and second ($f' = 2f$) harmonic frequency. Those components may be extracted with different filters in the postprocessing step. For SD-FMR, this DC component is called the V_{DC} voltage and, in the experiment, it is separated from the AC components using a bias-T filter [26,27].

In the simulation setup, we compute V_{DC} analogously to the experiment: a sinusoidal current I_{RF} with microwave frequency f is applied along the x axis, which in turn generates a tangent Oersted field H_{Oe}. This guides oscillations of the magnetization and time-varying resistance, $R_{\mathrm{xx}}(t)$ and $R_{\mathrm{xy}}(t)$. Multiplying the sinusoidal current excitation and the resistance produces a voltage $V(t)$, that akin to experiment, has the DC and AC components. To separate the DC component, we filter the voltage signal with a digital low pass filter (LPF). Taking a mean of the LPF-filtered voltage signal yields one V_{DC} value for each magnetic field and frequency.

D. Harmonic Hall voltage detection

We determine the spin torque components with harmonic Hall voltage measurements in the low-frequency regime. The

established methods use either magnetic field dependence [19] or angular dependence [28] to analyze the first and second harmonic Hall voltage signals under AC (below the resonance frequency) excitation. CMTJ simulates these two approaches by extending the previously described SD-FMR method with a simple computation of phase and amplitude in the first and second harmonic, for the R_{xy} configuration. For low-frequency regimes, when the magnetization vector does not undergo large-angle variations, the results happen to be sufficiently close.

In our simulations, we follow the SOT formulation as described in Eq. (1). At a low frequency, below the resonance, we perform a field scan, where at each field step the system is excited with a sinusoidal torque signal, with separate amplitudes for damping- and fieldlike torques. We compute the R_{xy} magnetoresistance using Eq. (3), and calculate the fast Fourier transform (FFT) of the mixing voltage signal to obtain the amplitude and phase. We remove the offset from the experiment and simulation data for the first harmonic, and we convert the second harmonic phase from radian to voltage. Then, following the lock-in [29] operation, we first take the cosine of the simulated phase and then multiply by the amplitude of the signal at that second harmonic. In such a way, we obtain the amplitudes consistent with what we get from the experiment, while keeping all simulation parameters realistic (layer parameters, applied current density, and torques come well within the range observed during the experiment measurement).

III. RESULTS

We now turn to a comparison of numerical simulations conducted using CMTJ with the experimental results obtained on the Ta(5)/CoFeB(1.45)/MgO(2)/Ta(1) structure (thickness in nanometers). The system has been patterned into Hall bars, enabling both static and low-frequency longitudinal and transverse resistance measurements as well as magnetization dynamics characterization using the SD-FMR technique. The Ta underlayer was chosen such that it generates significant SOT and SMR [30]. The selected CoFeB thickness results in net perpendicular anisotropy induced by the dominating interfacial anisotropy component. For low-frequency R_{xx} and R_{xy} measurements, the excitation voltage was fixed to 1 V. High-frequency measurements were performed with the radio frequency (rf) signal of power $P = 16$ dBm. The details of the sample fabrication are presented in Ref. [31].

The process of numerical harmonic detection is composed of several steps. First, we compute the magnetoresistance parameters that will serve as a basis for our further simulations. In particular, we use our model to fit the magnetoresistance parameters using the angular dependencies of the resistance in the saturating magnetic field. This permits us to determine the resistance values: AMR, SMR, and AHE. Then, we obtain the magnetization, saturation, and magnetic anisotropy from the R-H loops. In the next step, we simulate the SD-FMR maps for the R_{xx} and R_{xy} configurations using previously determined parameters. We compare them with the dispersion relations from the SD-FMR measurements for those two electrical configurations. Finally, using all the parameters that were determined in the previous steps, we reproduce the first and second harmonics measurements.
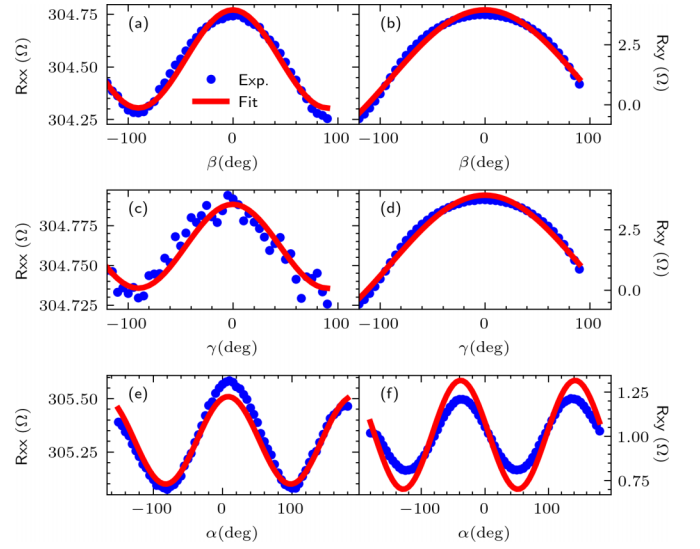

FIG. 2. Comparison measurements and simulations for (a),(c),(e) R_{xx} and (b),(d),(f) R_{xy} at the rotations of the saturating magnetic field in α, β, and γ angles. Experimental results are marked with blue dots; red lines represent simulation.

A. Resistance measurement

To determine the magnetoresistance and magnetic parameters of the investigated sample, we perform a series of angular measurements in the saturating magnetic field and field scans at preset directions. Angular dependencies of R_{xx} and R_{xy} measured at magnetic field of 1 T sweeping at α, β, and γ angles are shown in Fig. 2. The red line represents the results obtained from the numerical model, with electrical parameters listed in Table I. A small discrepancy from a perfect sine waveform may be caused due to the FM layer being not fully saturated.

Figure 3 shows the experimental results of R_{xx} and R_{xy} as a function of magnetic field applied along an xy plane at $0°$ and $45°$. Corresponding simulations reproduced by CMTJ are depicted as red lines in the same figure. The higher switching field in the simulated loops observed for the $R_{xy}(H)$ dependency may be explained by the thermally activated magnetic domain switching [32] that we did not take into account in this version of the model. The following parameters

TABLE I. Optimal parameters used in the simulations.

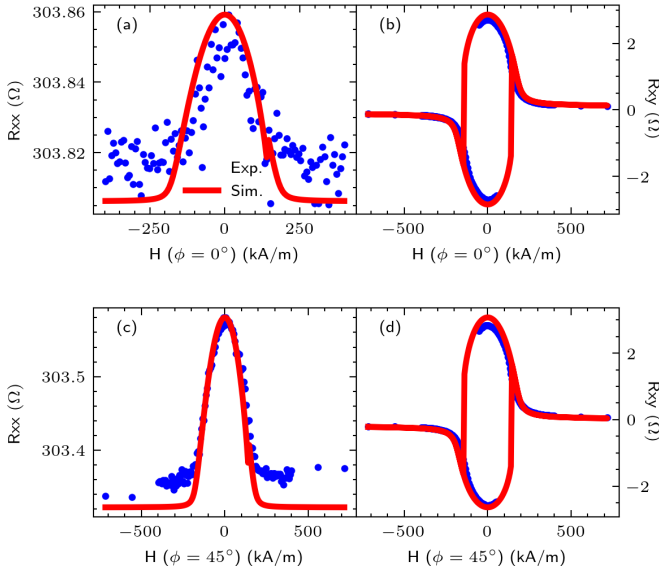| Parameter	Value	Unit
$\mu_0 M_s$	0.525	T
K_u	0.154	MJ/m³
α_G	0.03	
t_{FM}	1.45	nm
ΔR_{SMR}	−0.464	Ω
ΔR_{AMR}	−0.053	Ω
ΔR_{AHE}	−5.71	Ω
w	30	μm
l	20	μm
$|H_{DL}|$	420	A/m
$|H_{FL}|$	574	A/m

FIG. 3. Comparison measurements' data points and simulations for (a),(c) R_{xx} and (b),(d) R_{xy} at sweeps of the in-plane ($\theta = 90°$) magnetic field at $\phi = 0°$ and $45°$. Blue connected dots indicate the experimental results, whereas the solid red line represents simulation results obtained with CMTJ.

reproduce experimental findings to a good degree of precision: the saturation magnetization $\mu_0 M_s = 0.525\,\text{T}$, the nominal thickness of CoFeB (t_{FM}) of 1.45 nm, the magnetic perpendicular anisotropy $K_u = 0.154\,\text{MJ/m}^3$, and resistance parameters of $\Delta R_{AMR} = -0.053\,\Omega$, $\Delta R_{SMR} = -0.464\,\Omega$, and $\Delta R_{AHE} = -5.71\,\Omega$, all summarized in Table I for convenience.

B. Magnetization dynamics

The magnetization dynamics was measured using the SD-FMR technique with a fixed RF power of 16 dBm, frequency between 1 and 18 GHz, and a magnetic field swept between 0 and 600 kA/m. An example of the measured and simulated spectra for the transverse and longitudinal magnetoresistance measurement configurations is presented in Fig. 4. In Fig. 4, we also plot the individual resonance modes of both configurations (R_{xx} and R_{xy}) in a selected range of higher frequencies (12–16 GHz), then depicted for the whole frequency range in the form of dispersion relations in Fig. 5. Generally, the half widths as well as the resonance peaks of the simulated runs (the dashed red line) remain in good agreement with the experiment marked with colored dots. The colored lines represent the Lorentz fit, which was computed with the following formula:

$$V_{DC}(H) = A_S L + A_A D, \qquad (4)$$

$$L = \frac{\Delta H^2}{(H - H_r)^2 + \Delta H^2}, \quad D = \frac{\Delta H (H - H_r)}{(H - H_r)^2 + \Delta H^2}, \qquad (5)$$

where A_S and A_A are amplitudes of the symmetric and antisymmetric components of the resonance line, H_r is the resonance field, and ΔH is the linewidth.
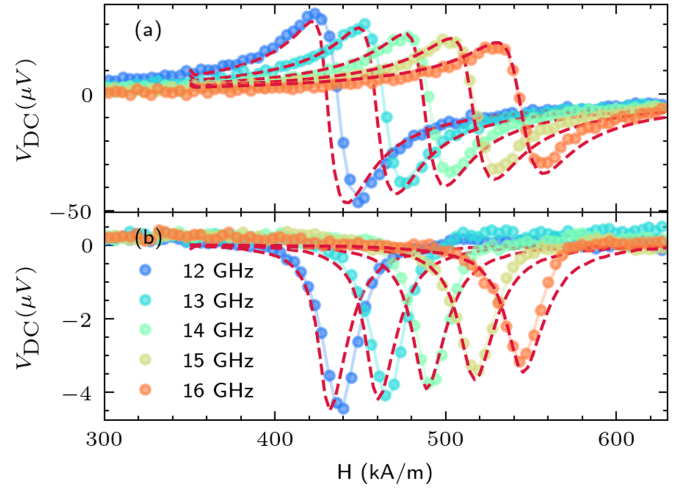

FIG. 4. Examples of V_{DC} voltage measured as a function of external magnetic field applied in plane ($\theta = 90°$) measured at (a) R_{xy} (H applied at $\phi = 0°$) and (b) R_{xx} (H applied at $\phi = 45°$) electrical configuration for frequencies ranging from 12 to 16 GHz. Colored points are experimental data; the Lorentz fits to (4) are marked with a solid line of the same color. Simulations corresponding to each frequency are marked with red dashed lines; for the R_{xx} configuration, the current was 0.4 mA, while for the R_{xy} one, the current was 0.75 mA. Finally, we get the best agreement with $\alpha_G = 0.03$, and the other simulation parameters follow Table I.

C. Harmonic Hall detection

In the experimental setup, we are primarily interested in measuring the effective torque efficiencies (ξ), for both the DL and FL. Those efficiencies may be easily calculated given the values of H_{DL} and H_{FL} fields at a current density j_e [22],

$$\xi_{DL/FL} = \frac{2e\mu_0 M_s}{\hbar} \frac{t_{FM} H_{DL/FL}}{j_e}, \qquad (6)$$
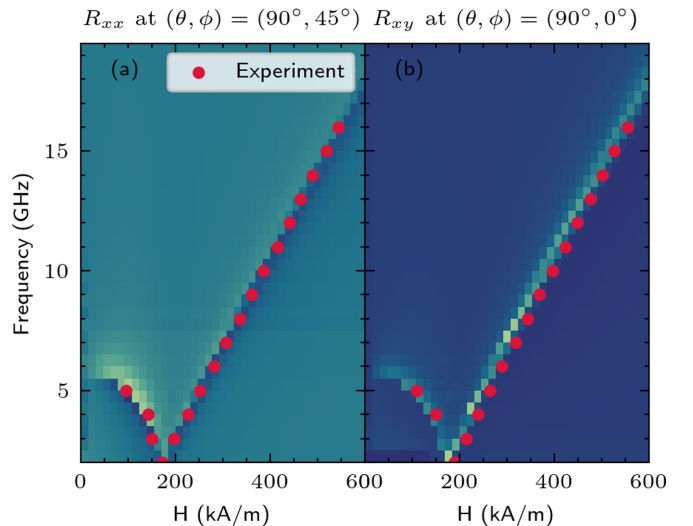

FIG. 5. Dispersion relations of SD-FMR measurements for (a) longitudinal and (b) transverse. Red dots represent the experimental relations of the dispersion obtained for both configurations.
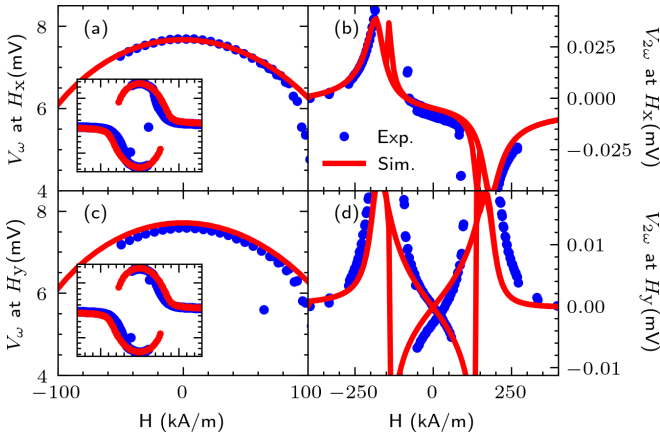
FIG. 6. The best fit for first and second harmonics in the following arrangements: (a),(b) H_x with $\theta = 90°$, $\phi = 0°$ and (c),(d) H_y with $\theta = 90°$, $\phi = 90°$. Blue dots represent the experimental data, and the red lines depict the simulation results from CMTJ. (a),(c) The first harmonic response; (b),(d) the second harmonic response. The primary fitting variables are the curvature of the quadratic region in the first harmonics and the slope in the linear section in the second harmonic curve. Inset: the complete view of the first harmonic voltage in the field range from -400 to $400 \, \mathrm{k}\frac{A}{m}$.

where $\mu_0 M_s$ is the magnetization saturation and t_{FM} is the thickness of the ferromagnetic layer. The H_{DL} and H_{FL} fields may be computed from the first V_ω and and second $V_{2\omega}$ harmonic responses in two arrangements: longitudinal (L), later called H_x, and transversal (T), marked H_y. For instance, one can obtain H_{DL} with the following formula:

$$H_{DL} = -\frac{2}{\zeta}\frac{\rho_L \pm 2\kappa\rho_T}{1 - 4\kappa^2}, \qquad (7)$$

where κ is the ratio of planar Hall effect (PHE) and AHE resistance and $\rho_{L/T} = \partial V_{2\omega}/\partial H_{ext}^{L/T}$ for the longitudinal L and transverse T arrangement, respectively. In the H_x (longitudinal) setting, we apply the external field at $\phi = 0°$ and $\theta = 90°$, whereas for the H_y (transverse) arrangement, we have $\phi = 90°$ and $\theta = 90°$. The parameter $\zeta = \partial^2 V_\omega/\partial H_{ext}^2$ is obtained by fitting the low-regime region of the first harmonic, V_ω, to a quadratic function. The $V_{2\omega}$ should resemble a linear function in the same low-field regime as in the case of the first harmonic. We fit that region to obtain the function slope ρ for both H_x and H_y arrangements. Interchanging the subscripts L and T in Eq. (7) yields the value of H_{FL}.

The parameters $\mu_0 M_s$ and K_u were not adjusted in this step and the values of the torques were determined from the experimental data using Eq. (7). We show the results of the best fit to the experimental data in Fig. 6. The computed torque fields are $|H_{DL}| = 420 \, \frac{A}{m}$ and $|H_{FL}| = 574 \, \frac{A}{m}$ at 5 mA current, with the remaining parameters of the simulated structure taken from Table I. As the experimental rotations may have a slight angular error, we emulate that in the simulation by allowing for the θ and ϕ (as per Fig. 1) angle to deviate from the ideal up to $\approx 3°$.

IV. PARAMETRIC ANALYSIS

Finally, after introduction of the model and presentation of the best fits to the experimental results, we turn to the discussion of the parametric analysis. Specifically, we performed the analysis of $\mu_0 M_s$, K_u, and θ by scanning each within a $\pm 5\%$ margin respective to the value of the best fit to the experimental data (Fig. 7). The deviations of the polar angle cause little effect for the second harmonics in the region of interest (the linear region in the low-field regime), but may contribute to large changes in the first harmonic at higher field magnitudes. From contrasting $\mu_0 M_s$ and K_u scans, we see that the former has a much greater impact on both harmonic Hall voltage components than the latter—specifically, much greater widening/stretching of the quadratic region in the first harmonic and the significant increase/decrease of the slope in the second harmonics in both arrangements. Furthermore, manipulating $\mu_0 M_s$ has an inverse effect of that of K_u. Namely, an increase in $\mu_0 M_s$ may potentially be compensated by the adequate decrease of the K_u.

We then turn to the analysis of the behavior of the FL and DL torques when their values are being varied while all other parameters stay constant (note that the magnitude of change is now $\pm 20\%$). Figure 8 depicts this attempt at evaluating the influence of torque modifications across different applied field arrangements. First, we observe little to no change in the first harmonic response under either FL- or DL-torque variation. Altering the DL torque yields a significant deviation of the slope of the linear region in the longitudinal arrangement towards lower field regimes. However, manipulating with the DL torque causes no visible alterations in the transverse arrangement. The situation flips when the FL torque is varied while the DL torque is kept constant—we notice a visible decrease in the slope values over the crossing linear regions in the H_y arrangements, but no remarkable changes in the H_x setting. Together with the analysis of Fig. 7, we may posit that in our experiments, the first harmonic was entirely affected by the values of θ, $\mu_0 M_s$, or K_u. The inspection of the second harmonic components becomes more involved, as the linear regions may be compensated by manipulating with $\mu_0 M_s$, K_u, but also the corresponding torque component and, to a lesser degree, the θ angle also. Fortunately, we can fix either $\mu_0 M_s$ or K_u by fitting to the dispersion relation first, thus reducing the initial problem of the second harmonic to exclusively tailoring H_{FL} or H_{DL} components.

In Fig. 9, we plot the mean-squared error (MSE) between the parameters taken from Table I and other simulations with parameters taken within some neighborhood of the optimal ones. The color indicates the magnitude of the MSE, with brighter regions corresponding to a lower MSE. In Fig. 9(a), we see that there is a line of minimal MSE for a range of $(\mu_0 M_s, K_u)$ pairs. For a small variation of the K_u, as is the case in Fig. 9(b), we may calculate the corresponding $\mu_0 M_s$ values based on a linear model. Then, we overlay several SD-FMR lines computed based on those pairs to obtain Fig. 9(a). We see that within a good approximation, the $(\mu_0 M_s, K_u)$ pairs produce the same SD-FMR line, which supports the idea that there are several families of parameters that may be eligible for a fit. Hence, it is of primary importance to cross-check those values against the dispersion relation, as presented in
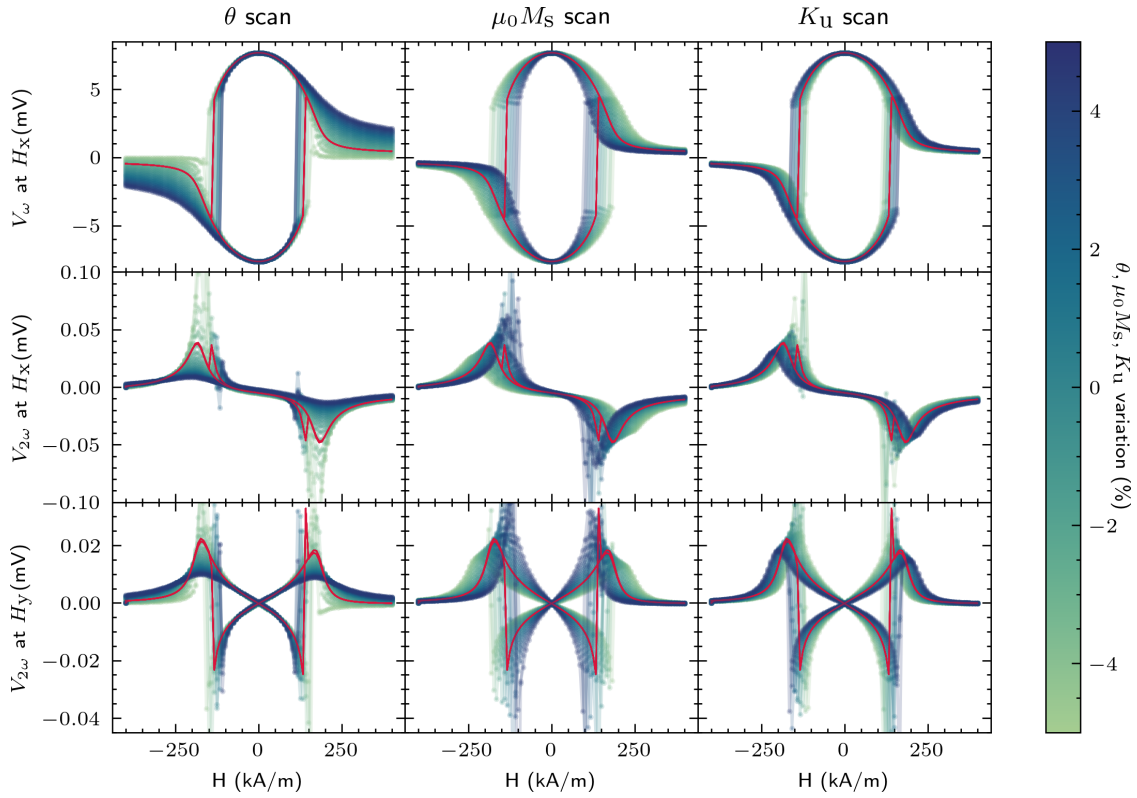
FIG. 7. The figure presents the influence of parameters $\mu_0 M_s$, K_u, and θ on the first and second harmonic scans. Red lines represent the original curve simulated with the parameters from Table I. We simulated the system by varying the selected parameter, but keeping the rest fixed. We see that increasing $\mu_0 M_s$ reveals an inverse effect to increasing K_u, but the rate of change for the latter is much smaller than the one for the former. The range of the θ scan was centered around $94.8° \pm 5\%$; for the $\mu_0 M_s$, K_u scans, the default angle was $\theta = 92°$.
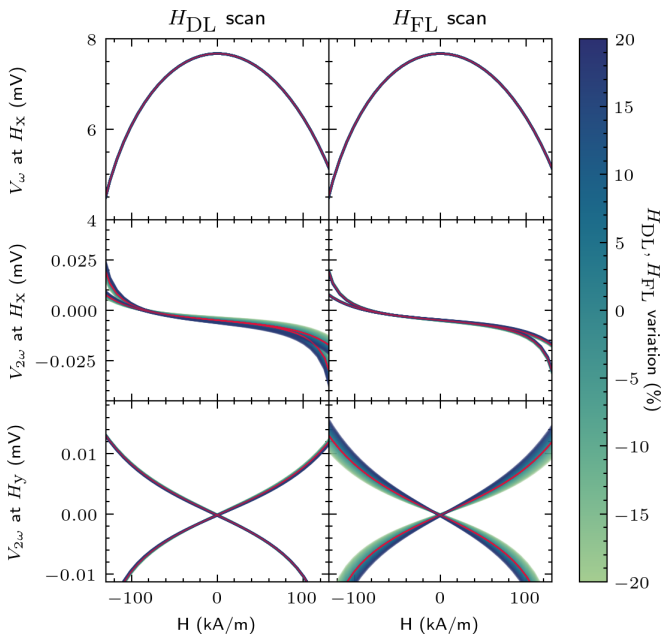

FIG. 8. The torque variation at different field arrangements. Clearly, H_{DL} influences only the second harmonic at the H_x setting, but has no strong effect when the sample is subjected to field at H_y. Conversely, H_{FL} has a strong impact on the angle of line crossing in the H_y arrangement, but causes little changes in the H_x setup. Neither of the torque contributions significantly affects the first harmonic components.

Fig. 5. A good approximation of $\mu_0 M_s$ from, e.g., vibrating sample magnetometer (VSM) measurements, helps to reduce the exhaustive search and narrow the range of feasible values of the K_u parameter. To sum up, the parametric analysis specfically shows that even a small variation of the saturation
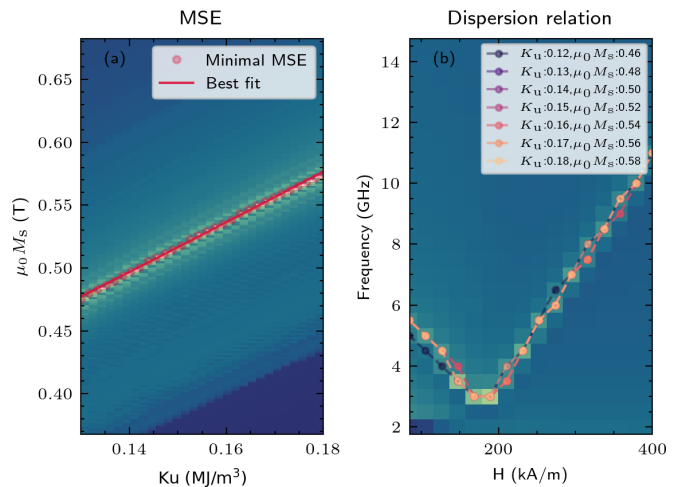

FIG. 9. (a) The map of the MSE respective to the SD-FMR generated with Table I. The brighter the color, the better the minimum (smaller distance between two curves). (b) The resulting dispersion relation for a range of K_u (in MJ/m^3) parameters and respective $\mu_0 M_s$ (in T) values computed from the fitted function in the right panel.

magnetization may lead to significant over- or underestimation of the SOT parameters.

Combining the observations made regarding Fig. 8 and Fig. 7, one may try to optimize for an optimal effective spin-Hall angle. By knowing how the change in the $(\mu_0 M_s, K_u)$ pair affects the quadratic region of the first harmonic and the linear region of the second harmonic, it is possible to relate that change to the dependency from Fig. 8 and thus conclude the effective impact on the spin-Hall angle, as computed in Eq. (6).

V. CONCLUSIONS

To conclude, we demonstrated a stable, reproducible method for modeling a wide spectrum of static and dynamic experimental techniques using the macrospin numerical model. All parameters obtained from the experimental angular and field dependencies are consistent with magnetoresistance dependencies, SD-FMR, and harmonics detection measurements. Furthermore, we performed scans of parameters such as $\mu_0 M_s$, K_u, and θ, each within $\pm 5\%$, to gain insight into the effect that those parameters have on the shape of the harmonics. From that, we show a strong dependency of both V_ω and $V_{2\omega}$ curves on $\mu_0 M_s$, much more potent than that of K_u, which may have a significant bearing on the resultant Hall angle. However, here we presented only a small portion of the functionality offered by our model. Primarily, we focused on the determination of spin-torque effective fields H_{DL} and H_{FL}, which has become an important problem in practical spintronics applications over recent years. CMTJ has more to offer in modeling multilayer spintronic devices and spintronics circuits, where several devices are coupled to each other via the mechanism of either electric or dipole coupling. Future work may also focus on automatic fitting parameters with Bayesian optimization, significantly reducing the need for manual supervision of fit quality. Specifically, an interesting direction of research is optimizing for minimizing the switching current in STT- or SOT-based devices with a given set of parameters such as spin-Hall angle, magnetization saturation, and anisotropy. Furthermore, with the CMTJ package, one can also try to minimize the microwave oscillation linewidth and maximize the oscillation power of STT- or SOT-based nano-oscillators by proposing a set of realistic magnetic parameters of the multilayer system.

ACKNOWLEDGMENTS

APPENDIX: REFORMULATING LLGS EQUATION TO THE LL FORM

In this section, we outline the steps to obtain the numerically useful LL form of the LLGS equation, wherein there is no implicit $\frac{d\mathbf{m}}{dt}$,

$$\frac{d\mathbf{m}}{dt} = -\gamma_0 \mathbf{m} \times \mathbf{H}_{eff} + \alpha_G \mathbf{m} \times \frac{d\mathbf{m}}{dt}$$
$$- \gamma_0 |H_{FL}| \mathbf{m} \times \mathbf{p} - \gamma_0 |H_{DL}| \mathbf{m} \times \mathbf{m} \times \mathbf{p}. \quad (A1)$$

We follow [33]. First, applying $\mathbf{m} \times$ to Eq. (A1) yields

$$\mathbf{m} \times \frac{d\mathbf{m}}{dt} = -\gamma_0 \mathbf{m} \times \mathbf{m} \times \mathbf{H}_{eff} + \alpha_G \mathbf{m} \times \mathbf{m} \times \frac{d\mathbf{m}}{dt}$$
$$- \gamma_0 |H_{FL}| \mathbf{m} \times \mathbf{m} \times \mathbf{p} - \gamma_0 |H_{DL}| \mathbf{m}$$
$$\times \mathbf{m} \times \mathbf{m} \times \mathbf{p}. \quad (A2)$$

After some simplification of (A2), we obtain

$$\mathbf{m} \times \frac{d\mathbf{m}}{dt} = -\gamma_0 \mathbf{m} \times \mathbf{m} \times \mathbf{H}_{eff} - \alpha_G \frac{d\mathbf{m}}{dt}$$
$$- \gamma_0 |H_{FL}| \mathbf{m} \times \mathbf{m} \times \mathbf{p} + \gamma_0 |H_{DL}| \mathbf{m} \times \mathbf{p}. \quad (A3)$$

Substituting the right-hand side of (A3) into (A1) in lieu of the $\mathbf{m} \times \frac{d\mathbf{m}}{dt}$ term leads to

$$\frac{d\mathbf{m}}{dt} = -\gamma_0 \mathbf{m} \times \mathbf{H}_{eff} + \alpha_G \left[-\gamma_0 \mathbf{m} \times \mathbf{m} \times \mathbf{H}_{eff} \right.$$
$$\left. - \alpha_G \frac{d\mathbf{m}}{dt} - \gamma_0 |H_{FL}| \mathbf{m} \times \mathbf{m} \times \mathbf{p} + \gamma_0 |H_{DL}| \mathbf{m} \times \mathbf{p} \right]$$
$$- \gamma_0 |H_{FL}| \mathbf{m} \times \mathbf{p} - \gamma_0 |H_{DL}| \mathbf{m} \times \mathbf{m} \times \mathbf{p}.$$

Gathering all the $\frac{d\mathbf{m}}{dt}$ terms produces

$$\frac{d\mathbf{m}}{dt}(1 + \alpha_G^2) = -\gamma_0 \mathbf{m} \times \mathbf{H}_{eff} - \alpha_G \gamma_0 \mathbf{m} \times \mathbf{m} \times \mathbf{H}_{eff}$$
$$- \gamma_0 |H_{FL}| [\mathbf{m} \times \mathbf{p} + \alpha_G \mathbf{m} \times \mathbf{m} \times \mathbf{p}]$$
$$- \gamma_0 |H_{DL}| [\mathbf{m} \times \mathbf{m} \times \mathbf{p} - \alpha_G \mathbf{m} \times \mathbf{p}].$$

Rearranging the torque terms gives

$$\frac{d\mathbf{m}}{dt} = \frac{-\gamma_0}{1 + \alpha_G^2} [\mathbf{m} \times \mathbf{H}_{eff} + \alpha_G \mathbf{m} \times \mathbf{m} \times \mathbf{H}_{eff}] + \frac{-\gamma_0}{1 + \alpha_G^2} [|H_{FL}| [\mathbf{m} \times \mathbf{p} + \alpha_G \mathbf{m} \times \mathbf{m} \times \mathbf{p}]$$
$$+ |H_{DL}| [\mathbf{m} \times \mathbf{m} \times \mathbf{p} - \alpha_G \mathbf{m} \times \mathbf{p}]].$$

The last part of Eq. (A4) can be rearranged to

$$\frac{d\mathbf{m}}{dt} = \frac{-\gamma_0}{1 + \alpha_G^2} [\mathbf{m} \times \mathbf{H}_{eff} + \alpha_G \mathbf{m} \times \mathbf{m} \times \mathbf{H}_{eff}] + \frac{-\gamma_0}{1 + \alpha_G^2} [\mathbf{m} \times \mathbf{p}(|H_{FL}| - \alpha_G |H_{DL}|)$$
$$+ \mathbf{m} \times \mathbf{m} \times \mathbf{p}(|H_{DL}| + \alpha_G |H_{FL}|)]. \quad (A4)$$

What becomes evident in this LL form of the LLG equation is the mixing of the torques with damping as the scaling factor. The fieldlike term, for instance, becomes $|H_{\text{FL}}| - \alpha|H_{\text{DL}}|$. We may neglect the second part of that term for small values of $|H_{\text{FL}}| \gg \alpha|H_{\text{DL}}|$. For numerical computation, we use Eq. (A4).

---

[1] B. Dieny, I. L. Prejbeanu, K. Garello, P. Gambardella, P. Freitas, R. Lehndorff, W. Raberg, U. Ebels, S. O. Demokritov, J. Akerman, A. Deac, P. Pirro, C. Adelmann, A. Anane, A. V. Chumak, A. Hirohata, S. Mangin, S. O. Valenzuela, M. C. Onbaşlı, M. d'Aquino, G. Prenat, G. Finocchio, L. Lopez-Diaz, R. Chantrell, O. Chubykalo-Fesenko, and P. Bortolotti, Opportunities and challenges for spintronics in the microelectronics industry, Nat. Electron. **3**, 446 (2020).

[2] S. Bhatti, R. Sbiaa, A. Hirohata, H. Ohno, S. Fukami, and S. Piramanayagam, Spintronics based random access memory: A review, Mater. Today **20**, 530 (2017).

[3] S. Ikegawa, F. B. Mancoff, J. Janesky, and S. Aggarwal, Magnetoresistive random access memory: Present and future, IEEE Trans. Electron Devices **67**, 1407 (2020).

[4] A. Hirohata, K. Yamada, Y. Nakatani, I.-L. Prejbeanu, B. Diény, P. Pirro, and B. Hillebrands, Review on spintronics: Principles and device applications, J. Magn. Magn. Mater. **509**, 166711 (2020).

[5] S. Manipatruni, D. E. Nikonov, C.-C. Lin, T. A. Gosavi, H. Liu, B. Prasad, Y.-L. Huang, E. Bonturim, R. Ramesh, and I. A. Young, Scalable energy-efficient magnetoelectric spin–orbit logic, Nature (London) **565**, 35 (2019).

[6] D. Ralph and M. Stiles, Spin transfer torques, J. Magn. Magn. Mater. **320**, 1190 (2008).

[7] A. Brataas, A. D. Kent, and H. Ohno, Current-induced torques in magnetic materials, Nat. Mater. **11**, 372 (2012).

[8] A. Manchon, J. Železný, I. M. Miron, T. Jungwirth, J. Sinova, A. Thiaville, K. Garello, and P. Gambardella, Current-induced spin-orbit torques in ferromagnetic and antiferromagnetic systems, Rev. Mod. Phys. **91**, 035004 (2019).

[9] C. Zhang, Y. Takeuchi, S. Fukami, and H. Ohno, Field-free and sub-ns magnetization switching of magnetic tunnel junctions by combining spin-transfer torque and spin–orbit torque, Appl. Phys. Lett. **118**, 092406 (2021).

[10] Z. Chen, C. Pan, N. Wang, M. Qiu, T. Lin, J. Liu, S. Li, P. Han, J. Shi, K. Ando *et al.*, Manipulation of perpendicular exchange bias and spin-orbit torques via mgo in pt/co/mgo films, J. Magn. Magn. Mater. **507**, 166822 (2020).

[11] L. Liu, C.-F. Pai, Y. Li, H. Tseng, D. Ralph, and R. Buhrman, Spin-torque switching with the giant spin Hall effect of tantalum, Science **336**, 555 (2012).

[12] C. Song, R. Zhang, L. Liao, Y. Zhou, X. Zhou, R. Chen, Y. You, X. Chen, and F. Pan, Spin-orbit torques: Materials, mechanisms, performances, and potential applications, Prog. Mater. Sci. **118**, 100761 (2021).

[13] W. Skowroński, Ł. Karwacki, S. Zietek, J. Kanak, S. Łazarski, K. Grochot, T. Stobiecki, P. Kuświk, F. Stobiecki, and J. Barnaś, Determination of Spin Hall Angle in Heavy-Metal/co- fe- b-Based Heterostructures with Interfacial Spin-Orbit Fields, Phys. Rev. Applied **11**, 024039 (2019).

[14] P. Ogrodnik, K. Grochot, Ł. Karwacki, J. Kanak, M. Prokop, J. Chęciński, W. Skowroński, S. Ziętek, and T. Stobiecki, Study of spin-orbit interactions and interlayer ferromagnetic coupling in co/pt/co trilayers in wide range of heavy metal thickness, ACS Appl. Mater. Interfaces **13**, 47019 (2021).

[15] E. Grimaldi, V. Krizakova, G. Sala, F. Yasin, S. Couet, G. S. Kar, K. Garello, and P. Gambardella, Single-shot dynamics of spin–orbit torque and spin transfer torque switching in three-terminal magnetic tunnel junctions, Nat. Nanotechnol. **15**, 111 (2020).

[16] H. Zhou, C. Wang, Z. Li, Z. Wang, T. Liu, B. Wu, and W. Zhao, Design of an erasable spintronics memory based on current-path-dependent field-free spin orbit torque, AIP Adv. **10**, 015317 (2020).

[17] L. Liu, T. Moriyama, D. C. Ralph, and R. A. Buhrman, Spin-Torque Ferromagnetic Resonance Induced By the Spin Hall Effect, Phys. Rev. Lett. **106**, 036601 (2011).

[18] Q. Hao and G. Xiao, Giant Spin Hall Effect and Switching Induced By Spin-Transfer Torque in a w/co 40 fe 40 b 20/mgo Structure With Perpendicular Magnetic Anisotropy, Phys. Rev. Applied **3**, 034009 (2015).

[19] M. Hayashi, J. Kim, M. Yamanouchi, and H. Ohno, Quantitative characterization of the spin-orbit torque using harmonic hall voltage measurements, Phys. Rev. B **89**, 144425 (2014).

[20] J. Kim, J. Sinha, M. Hayashi, M. Yamanouchi, S. Fukami, T. Suzuki, S. Mitani, and H. Ohno, Layer thickness dependence of the current-induced effective field vector in ta| cofeb| mgo, Nat. Mater. **12**, 240 (2013).

[21] https://github.com/LemurPwned/cmtj.

[22] M.-H. Nguyen and C.-F. Pai, Spin–orbit torque characterization in a nutshell, APL Mater. **9**, 030902 (2021).

[23] J. Kim, P. Sheng, S. Takahashi, S. Mitani, and M. Hayashi, Spin Hall Magnetoresistance in Metallic Bilayers, Phys. Rev. Lett. **116**, 097201 (2016).

[24] N. Locatelli, V. Cros, and J. Grollier, Spin-torque building blocks, Nat. Mater. **13**, 11 (2014).

[25] A. A. Tulapurkar, Y. Suzuki, A. Fukushima, H. Kubota, H. Maehara, K. Tsunekawa, D. D. Djayaprawira, N. Watanabe, and S. Yuasa, Spin-torque diode effect in magnetic tunnel junctions, Nature (London) **438**, 339 (2005).

[26] J. C. Sankey, Y.-T. Cui, J. Z. Sun, J. C. Slonczewski, R. A. Buhrman, and D. C. Ralph, Measurement of the spin-transfer-torque vector in magnetic tunnel junctions, Nat. Phys. **4**, 67 (2008).

[27] S. Ziętek, P. Ogrodnik, M. Frankowski, J. Chęciński, P. Wiśniowski, W. Skowroński, J. Wrona, T. Stobiecki, A. Żywczak, and J. Barnaś, Rectification of radio-frequency current in a giant-magnetoresistance spin valve, Phys. Rev. B **91**, 014430 (2015).

[28] C. O. Avci, K. Garello, M. Gabureac, A. Ghosh, A. Fuhrer, S. F. Alvarado, and P. Gambardella, Interplay of spin-orbit torque and thermoelectric effects in ferromagnet/normal-metal bilayers, Phys. Rev. B **90**, 224427 (2014).

[29] Sr830 dsp lock-in amplifier manual, Stanford Research Systems (2011), https://www.thinksrs.com/downloads/pdfs/manuals/SR830m.pdf.

[30] M. Cecot, Ł. Karwacki, W. Skowroński, J. Kanak, J. Wrona, A. Żywczak, L. Yao, S. van Dijken, J. Barnaś, and T. Stobiecki, Influence of intermixing at the ta/cofeb interface on spin Hall angle in ta/cofeb/mgo heterostructures, Sci. Rep. **7**, 968 (2017).

[31] S. Łazarski, W. Skowroński, K. Grochot, W. Powroźnik, J. Kanak, M. Schmidt, and T. Stobiecki, Spin-orbit torque induced magnetization dynamics and switching in a cofeb/ta/cofeb system with mixed magnetic anisotropy, Phys. Rev. B **103**, 134421 (2021).

[32] M. Czapkiewicz, T. Stobiecki, and S. van Dijken, Thermally activated magnetization reversal in exchange-biased [pt/ co] 3/ pt/ ir mn multilayers, Phys. Rev. B **77**, 024416 (2008).

[33] J.-V. Kim, Spin-torque oscillators, in *Solid State Physics*, Vol. 63, edited by R. E. Camley and R. L. Stamps (Academic Press, San Diego, 2012), Chap. 4, pp. 217–294.